9D.4

Spectral retrieval of latent heating profiles from TRMM PR Data: Comparisons of lookup tables from two- and three-dimensional simulations

Shoichi Shige[1,*], Yukari N. Takayabu[2,3], Satoshi Kida[1], Wei-Kuo Tao[4] and Xiping Zeng[4,5]

[1]Department of Aerospace Engineering, Osaka Prefecture University, Osaka, Japan
[2]Center for Climate System Research, University of Tokyo, Tokyo, Japan
[4]Laboratory for Atmospheres, NASA/Goddard Space Flight Center, Greenbelt, Maryland
[5]Goddard Earth Sciences and Technology Center, University of Maryland, Baltimore County, Baltimore, Maryland

1. INTRODUCTION

The precipitation radar (PR) of the TRMM provides height information based upon the time delay of the precipitation-backscattered return power, and has enabled us to directly obtain vertical profiles of precipitation over the global Tropics (Kozu and Coauthors, 2001; Okamoto, 2003). The classification between convective and stratiform regions of mesoscale convective systems (MCS) became more straightforward utilizing observed precipitation profiles (Awaka et al., 1998). The accuracy of this classification is very important for estimating latent heating, because the differences of diabatic heating profiles that exist between convective and stratiform regions of MCSs (Houze, 1982; Johnson and Young, 1983). For convective regions of MCSs the heating profile has warming at all levels with a maximum at midlevels, whereas in stratiform regions there is a warming peak in the upper troposphere and a cooling peak at low-levels. The resulting MCS heating profile is positive at all levels, but with a maximum value in the upper troposphere.

Takayabu (2002) obtained a spectral expression of precipitation profiles to examine convective and stratiform rain characteristics statistically over the equatorial area (10^{o}N-10^{o}S) observed by the TRMM PR. In her study, all nadir data of PR2A25 version 5 (Iguchi et al. 2000) for the period of 1998-1999 were utilized and convective and stratiform precipitation were separated based on the TRMM PR version 5 2A23 convective-stratiform separation algorithm. Precipitation profiles with 0.3 mm hr^{-1} precipitation-top threshold were accumulated and stratified with precipitation-top heights (PTHs). Properties of convective rain profiles show near monotonic change with cumulative frequency. Stratiform rain profiles consist of two groups. One group consists of shallow stratiform rain profiles which are very weak and increase downward. The other group consists of anvil rain profiles, characterized by maximum intensity around the melting level, much less intensity above, and a downward decrease below as indicated in traditional radar observations.

Based on the results of spectral precipitation statistics of Takayabu (2002), the Spectral Latent Heating (SLH) algorithm has been developed for the TRMM PR (Shige et al. 2004, 2007, and 2008, hereafter Part I, II, and III). Heating profile lookup tables for the three rain types– convective, shallow stratiform, and anvil rain (deep stratiform with a melting level) were produced with numerical simulations of tropical cloud systems in Tropical Ocean Global Atmosphere (TOGA) Coupled Ocean–Atmosphere Response Experiment (COARE) utilizing a cloud-resolving model (CRM). For convective and shallow stratiform regions, the lookup table refers to the precipitation top height (PTH). For anvil region, on the other hand, the lookup table refers to the precipitation rate at the melting level instead of PTH.

The two-dimensional version of the GCE model was used in the previous studies. Real clouds and cloud systems are three-dimensional. The availability of exponentially increasing computer capabilities has resulted in three-dimensional CRM simulations for multiday periods with large horizontal domains becoming increasing prevalent. In this study, we compare look-up tables from the two- and three-dimensional CRM simulations.

2. APPROACH

Here the 2-D and 3-D versions of the Goddard Cumulus Ensemble (GCE) model (Tao and Simpson, 1993) are used. Numerical simulations were conducted with the large-scale forcing data from TOGA-COARE. In this paper, the SLH algorithm is also applied to PR data and the results will be compared to heating profiles derived diagnostically from sounding data of SCSMEX (Johnson and Ciesielski, 2002). We will show the results with Q_1 - Q_R (Q_{1R}), which

---

[*] Corresponding author address: Dr. Shoichi Shige, Department of Aerospace Engineering, Osaka Prefecture University, 1-1 Gakuen-cho, Sakai, Osaka, 599-8531 Japan; e-mail: shige@aero.osakafu-u.ac.jp

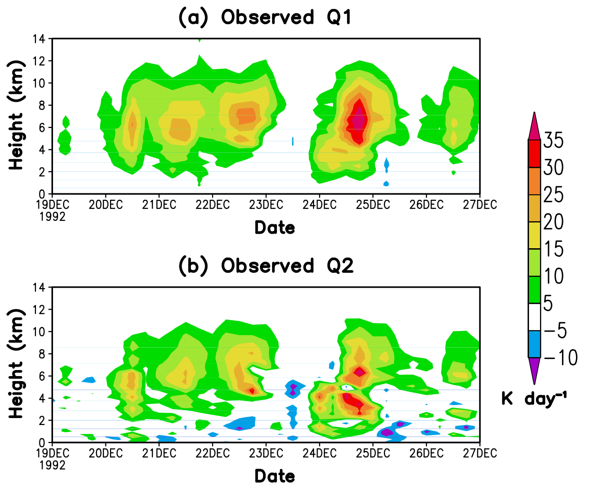

Figure 1: Time series of (a) Q_1 and (b) Q_2 profiles averaged over the TOGA COARE IFA region for the 19-26 December 1992 period derived diagnostically from soundings (Ciesielski et al., 2003).

is the important dynamically important quantity. Here Q_1 is the apparent heat source defined in diagnostic studies (Yanai et al., 1973; Yanai and Johnson, 1993), and Q_R is the cooling/heating rate associated with radiative processes.

3. RESULTS

3.1. General features

Figures 1, 2, and 3 show the time series of Q_1 and Q_2 profiles averaged over the TOGA COARE IFA region for the 19-26 December 1992 period derived diagnostically from soundings (Ciesielski et al., 2003), GCE 2-D simulations, and GCE 3-D simulations, respectively. There exisits larger temporal variability Q_1 and Q_2 profiles in the two-dimensional simulation than in the three-dimensional simulation, which is consistent with the results found by Grabowski et al. (1998), Donner et al. (1999) and Zeng et al.. (2007). Zeng and Coauthors (2007) suggested that the rapid fluctuation in surface precipitation (proportional to integrated Q_1 or Q_2) can be attributed to the fact that buoyancy dmping is sensitive to spatial smoothers in 2-D CRMs, but not in 3D ones.

The GCE 3-D model simulated Q_2 budget (Fig. 2b) is in better agreement with observations (Fig. 1b) in the lower-troposphere than its 2-D counterpart (Fig. 3b), as pointed out by Tao et al. (2000). The eddy moisture flux convergence is one of the major contributors to Q_2 while the contribution to the Q_{1R} budget by the eddy heat flux convergence is minor (Shige et al., 2008). Better agreement of the GCE 3-D model simulated Q_2 budget is due to the fact that the eddy moisture flux convergence is 3-D in nature.

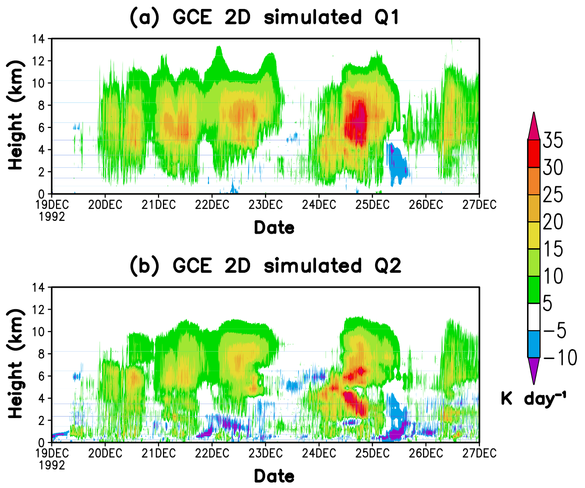

Figure 2: Same as Fig. 1, but for simulated by the GCE 2D model.

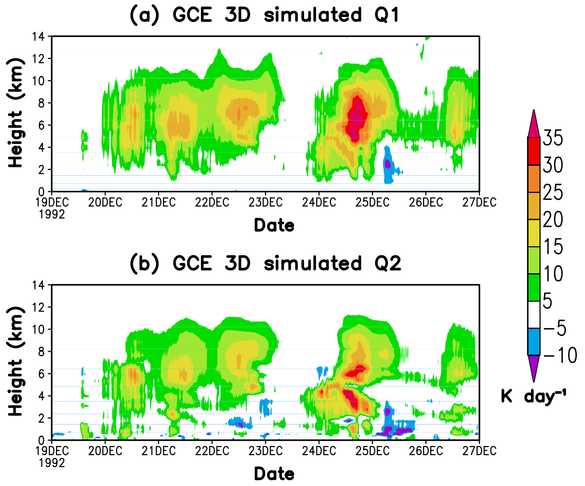

Figure 3: Same as Fig. 1, but for simulated by the GCE 3D model.

	Rainfall (mm day^{-1})	Stratiform (%)
GCE 2-D	19.86	43
GCE 3-D	18.98	40
Sounding	19.91	—

Table 1: Domain averaged surface rainfall amounts and stratiform percentage from the GCE 2-D model and 3-D one for the COARE episode. Rainfall estimated by sounding network is also shown.

Domain averaged surface rainfall amounts and stratiform percentage from the GCE 2-D model and 3-D one for the COARE episode are shown in Table 1. The model results indicate that stratiform rain percentage are not affected very much due to dimen-

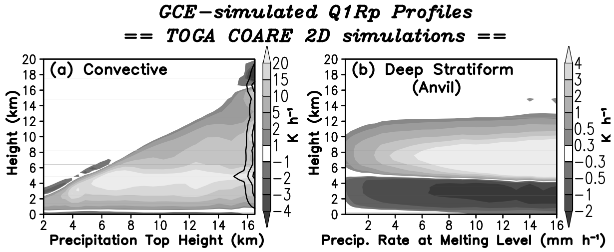

Figure 4: Lookup tables for the (a) convective and (b) deep stratiform (anvil) regions produced from the TOGA COARE 2D simulations.

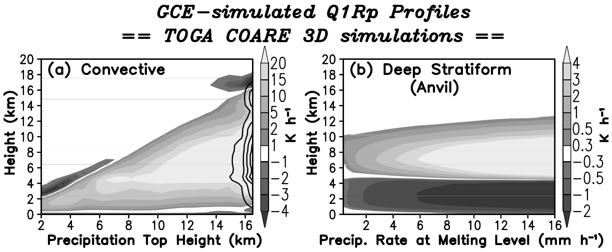

Figure 5: Same as Fig. 4, but produced from the TOGA COARE 3D simulations.

sionality. The reason for the similarity between the GCE 2-D and 3-D simlulations is that the same observed, large-scale advective tendencies of potential temperature, water vapor mixing ratio, and horizontal momentem were used as the main forcing in bothe 2-D and 3-D models.

3.2. Comparisons of lookup tables

Figure 4a shows a lookup table for convective rain produced from GCE 2D simulations. The GCE-simulated precipitation profiles with a 0.3 mm h^{-1} precipitation-top threshold and corresponding heating profiles are accumulated and averaged for each PTH with model grid intervals. Properties (i.e., shape and magnitude) of the convective heating profiles show near-monotonic changes with PTH. Heating top height is determined by the PTH. The shallow convective heating profiles (PTH $<$ 6 km) are characterized by cooling aloft due to an excess of evaporation over condensation, such as in tradewind cumulus (Nitta and Esbensen, 1974). Another interesting feature is that the convective heating profiles for the highest PTH are also characterized by cooling aloft. This feature is consistent with the strong cooling above mesoscale convective systems observed by Johnson and Kriete (1982) and Lin and Johnson (1996).

Figure 4b a lookup table for anvil (deep stratiform with a PTH higher than the melting level) rain. PR can measure the precipitation rate at the melting level as can surface-based radar (e.g. Leary and Houze 1979), although it cannot observe the PTH accurately enough in the upper-level regions of the anvils. Thus, for the anvil region, the lookup table refers to the precipitation rate at the melting level P_m instead of PTH (Part I). The anvil profiles with a PTH higher than the melting level are characterized by upper-level heating and lower-level cooling, which is also found in observations (e.g. Johnson and Young 1983). The upper level heating in these anvil regions is largely due to condensation and deposition, while the lower-level cooling is largely due to evaporation of raindrops and melting of ice particles (Tao et al., 1990). A set maximum height for Q_{1R} profiles can be seen around 12 km.

Figure 5a shows a lookup table for convective rain produced from GCE 3D simulations. As well as the lookup table from GCE 2D simulations, heating top height is determined by the PTH. The shallow convective heating profiles (PTH $<$ 6 km) are characterized by cooling aloft due to an excess of evaporation over condensation, and the convective heating profiles for the highest PTH are also characterized by cooling aloft.

On the other hand, differences in vertical structure (e.g., the level of maximum Q_{1Rp} heating) for a given PTH between lookup tables from GCE 2D simulations and GCE 3D simulations are distinct. In the lookup tables from GCE 2D simulations, the level of Q_{1R} heating peak shifts upward until PTH reaches 6 km, and then reach its plateau around the melting level (4.4 km). These results indicate that liquid water processes dominate in the GCE 2D simulations. In the lookup tables from GCE 3D simulations, the level of Q_{1R} heating peak for a PTH higher than 6 km is well above the melting level. These results indicate that ice water processes dominate in the GCE 2D simulations. A set maximum height for Q_{1R} profiles in the lookup table for the deep stratiform produced from the 3D simulations is lower than the 2D counterpart.

3.3. Comparison of Q_1 profiles over the SCSMEX NESA region

In Part II, the accuracy of the SLH-retrieved heating was evaluated by comparing with a rawinsonde-based analysis of diabatic heating for the SCSMEX NESA derived by Johnson and Ciesielski (2002). Figure 6 shows a comparison between SLH-retrieved Q_{1Rp} from version 6 of the TRMM PR data sets using lookup tables derived from GCE 2-D simulations and sounding-based Q_1 during the campaign's most convectively active period (May 15 – Jun 20 1998). Note that the total Q_{1Rp} profiles are not the same as in Part II, but are estimated using the Q_{1Rp} profile lookup tables derived from the TOGA-COARE simulations made with the TOGA COARE flux algorithm (Fairall et al., 1996; Wang et al., 1996) and a modification of conversion of cloud ice to snow

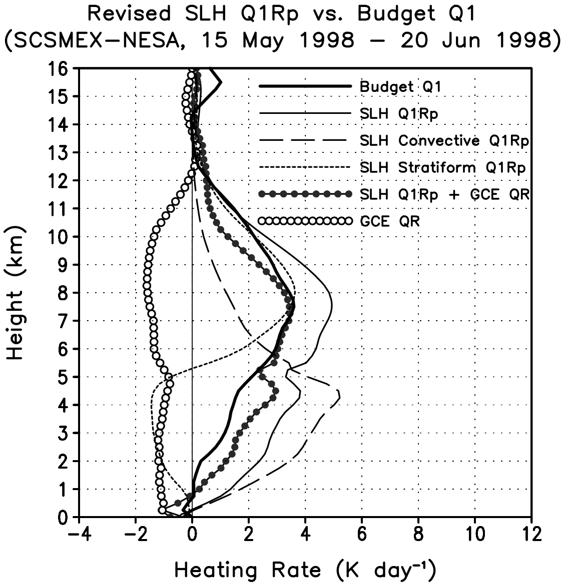

Figure 6: Heating from diagnostic calculations for SCSMEX (15 May - 20 June 1998) (Johnson & Ciesielski 2002) and the SLH algorithm using lookup tables derived from GCE 2D simulatioins.

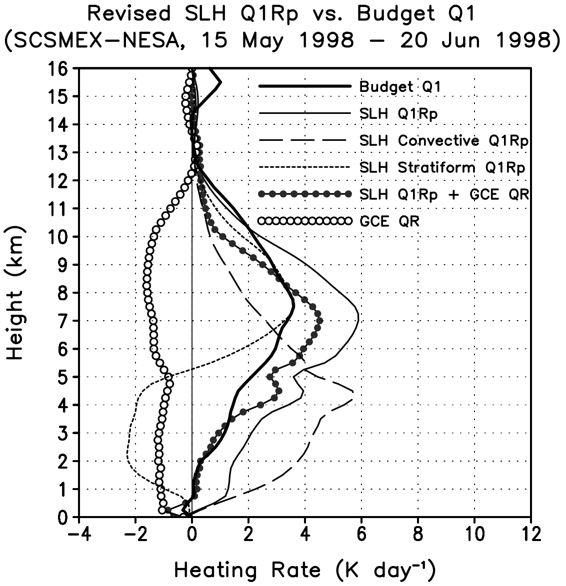

Figure 7: Same as Fig. 6, but for the SLH algorithm using lookup tables derived from GCE 3D simulations.

in the ice microphysics schemes (Tao et al. 2003). However, the differences are very small. As pointed out in Part II, key features of the vertical profiles agree well, particularly the level of maximum heating. The vertical profile of Q_R simulated by the GCE 2-D model for the SCSMEX periods (18–26 May 1998 and 2–11 June 1998) is shown on the left side of the figure. This Q_R component is added to the SLH-retrieved Q_{1Rp} estimates. The level of maximum heating of $Q_{1Rp} + Q_R$ and its magnitude are in very good agreement with the sounding-derived Q_1.

Figure 7 shows a comparison between SLH-retrieved Q_{1Rp} using lookup table derived from GCE 3-D simulations and sounding-based Q_1. The lookup table from GCE 3-D simulations results in less agreement between the SLH-retrieved Q_{1Rp} and sounding-based Q_1. The level of maximum heating of $Q_{1Rp} + Q_R$ is slightliy lower than that of the sounding-derived Q_1. The $Q_{1Rp} + Q_R$ magnitude at $z = 4$–8 km is larger than the sounding-derived Q_1.

4. DISCUSSIONS

To investigate less agreement between the SLH-retrieved Q_{1Rp} from 3D lookup table and sounding-based Q_1 than 2D counterpart, we examine the differences in the heating profiles between 2D and 3D. Figure 8 shows GCE-simulated Q_{1Rp} and precipitation profiles with selected PTHs of 3.1 km, 5.9 km, 10.2 km, and 14.0 km from the convective regions of 2D and 3D simulations. Note that the Q_{1Rp} profiles and precipitation profiles are normalized by the near-surface rainrate. The vertical structure (e.g., maximum heating level) of the convective heating profiles with PTH lower than 10 km does not vary beween 2D and 3D. However, the differences in convective heating profile shape between 2D and 3D increase with PTH higher than 10 km. The 3D convection has stronger heating above the melting level than the 2D convection does. Similarly, the differences in corresponding precipitation profile shape among cases also increases with PTH higher than 10 km. The 3D convection has stronger precipitation intensity above the melting level than 2D convection.

Figure 9 shows GCE-simulated Q_{1Rp} and precipitation profiles with selected P_ms of 2.0 mm hr^{-1}, 4.0 mm hr^{-1}, 8.0 mm hr^{-1}, and 16 mm hr^{-1} from the stratiform regions of 2D and 3D simulations. The lower-level cooling shape does not vary between 2D and 3D. However, the upper-level stratiform heating from 3D for smaller P_m (i.e. 2.0 mm hr^{-1} and 4.0 mm hr^{-1}) is weaker than 2D counterpart. The upper-level stratiform heating from 3D increases with P_m and is almost the same as 2D countetrpart. The number of pixels observed by PR is larger for weaker P_m. Thus, the SLH algorithm with 3D lookup table estimate weaker heating amplitude in stratiform heating, resulting in underesitamtion of the level of maximum heating.

Houze et al. (1980), Gamache and Houze (1983), and Chong and Hauser (1989) showed that the stratiform precipitation falling into the melting layer from the anvil cloud above is a combination of condensate generated in and carried over from the convec-

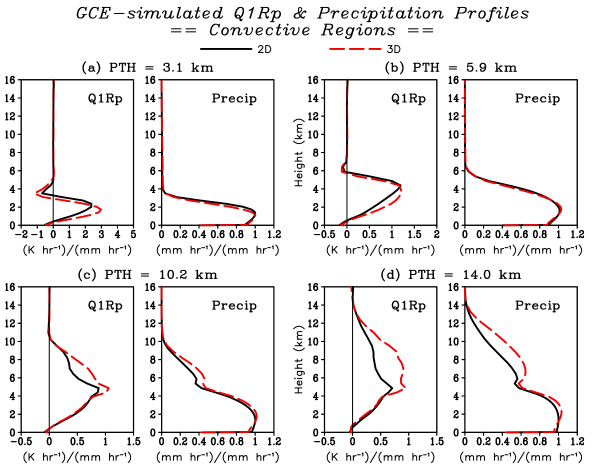

Figure 8: Ensemble-mean GCE-simulated Q_{1Rp} and precipitation profiles with the selected PTHs of (a) 3.1 km, (b) 5.9 km, (c) 10.2 km, and (d) 14km from the convective regions of 2D and 3D simulations. The Q_{1R} and precipitation profiles are normalized by near-surface rainrate.

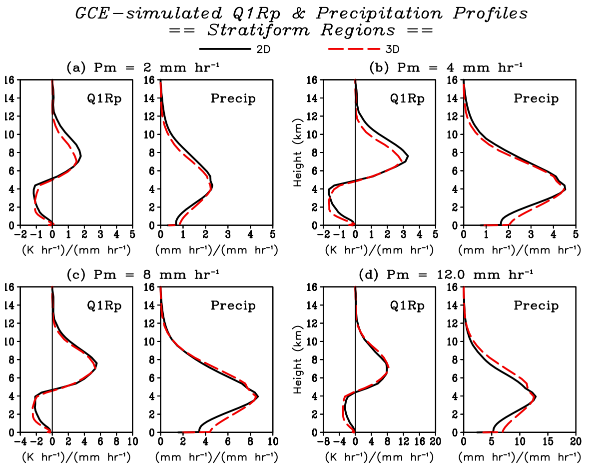

Figure 9: Ensemble-mean GCE-simulated Q_{1Rp} and precipitation profiles with the selected P_ms of (a) 2.0 mm hr^{-1}, (b) 4.0 mm hr^{-1}, (c) 8.0 mm hr^{-1}, and (d) 12 mm hr^{-1} from the stratiform regions of 2D and 3D simulations.

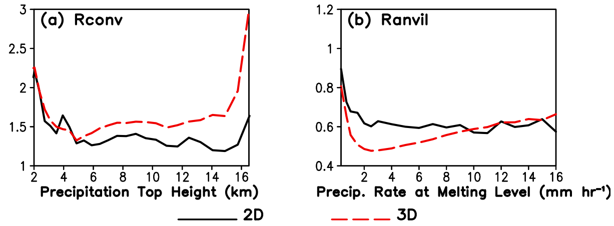

Figure 10: The ratios $\mathbf{R}_{conv}$ and $\mathbf{R}_{stra}$ defined as Eqs. (1) and (2) for lookup tables from GCE 2D and 3D simulations (Figs 4 and 5).

tive region plus condensate that is produced by the anvil region's own upward motion, analyzing the water budgets of a precipitating tropical mesoscale convective system. In order to evaluate this advection effect, we calculated following values for lookup tables from GCE 2D and 3D simulations (Figs 4 and 5).

$$\mathbf{R}_{conv} = \frac{C_p}{L_v}\int_0^{z_t} \rho\widetilde{Q_{1Rp}}(z)\triangle z \Big/ \widetilde{P}_s = 1+f \tag{1}$$

$$\mathbf{R}_{stra} = \frac{C_p}{L_v}\int_{z_m}^{z_t} \rho\widetilde{Q_{1Rp}}(z)\triangle z \Big/ \widetilde{P}_m = 1-f \tag{2}$$

Here, f is the fraction of the precipitation rate at the melting level, P_m, carried over from the convective region, and P_s is the precipitation rate at the observable lowest level and tildes denote the variables in the lookup table. For both 2D and 3D, $\mathbf{R}_{conv}$ are larger than unity and $\mathbf{R}_{stra}$ are smaller than unity (Fig. 10), which indicate the contribution to the anvil water budget made by the horizontal transfer of condensate from the convective region. There are big differences in $\mathbf{R}_{conv}$ and $\mathbf{R}_{stra}$ between 2D and 3D. $\mathbf{R}_{conv}$ for 2D decreases with PTH, but $\mathbf{R}_{conv}$ for 3D increases with PTH higher than 5 km. Total condensates generated in deep convection in 3D simulations are much larger than surface precipitation, which results in large $\mathbf{R}_{conv}$. On the other hand, $\mathbf{R}_{stra}$s from 3D are smaller than 2D counterparts in the range 1 mm h^{-1} $< \widetilde{P}_m \leq$ 8 mm h^{-1}. Thus, condensate carried over from the deep convection in 3D is larger than the 2D counterpart.

We obtained the spectral plots of convective precipitation profiles simulated in 2D and 3D (Fig. 11) to compare them against that of TRMM PR-observed precipitation profiles (Fig. 12). The 40 % of convective rain in 2D is shallow and congestus rain with PTHs lower than 4 km, consistent with TRMM PR observation. On the other hand, only 20 % of convective rain in 3D is shallow and congestus rain with PTHs lower than 4 km.

The GCE model results reported in Grabowski et al. (2006) showed that using a finer resolution (250 m versus 1000 m) resulted in a smoother transition to deep convection in diurnal convective growth during the TRMM Large-Scale Biosphere–Atmosphere (TRMM LBA) experiment in Brazil. Lang et al. (2007) showed that convective intensity in the 250 m simulation is steadier as opposed to being more pulse-like in the 1000-m run for convective systems during the TRMM LBA. They suggested the horizontal resolutions normally used to simulate deep convection (i.e., 1 km or coarser) are inadequate for the diurnal growth of convection in this type of environment and that finer resolutions are needed. Comparisons of lookup tables from 2D and 3D simulations in this study suggest that the horizontal resolution of 2 km are also inadequate for the oceanic convective sys-

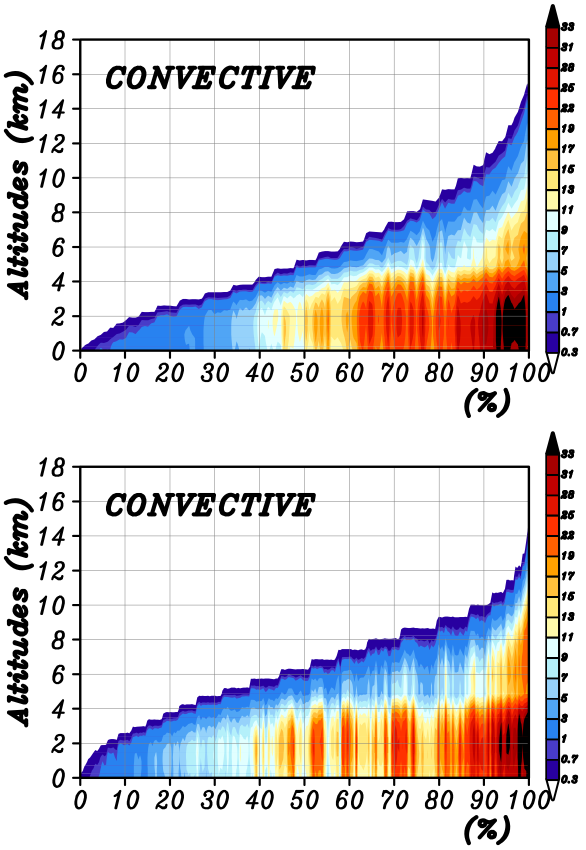

Figure 11: Cumulative plots of precipitation profiles stratified with precipitation top height (PTH) from convective region. (top) Simulated precipitation profiles from GCE 2D model. (bottom) Simulated precipitation profiles from GCE 3D model. The abscissa is cumulative frequency and the ordinate is altitude, and the precipitation rate is indicated with color shades. Thresholds of 0.3 mm hr^{-1} are used for the precipitation top detection.

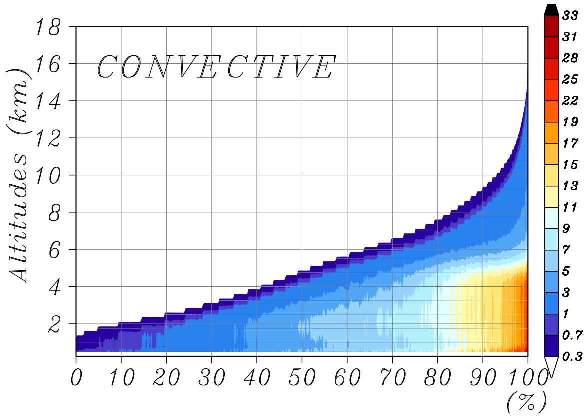

Figure 12: Same as Fig. 11, but for TRMM PR-observed convective precipitation profiles, utilizing all nadir data over ocean in 10^{o}N-10^{o}S belt for 3 years of 1998-2000 from PR2A25 version 5 with a reclassification of shallow, isolated rain (rain type 15 in product 2A-23) into convective rain. (Figure is from Part I.)

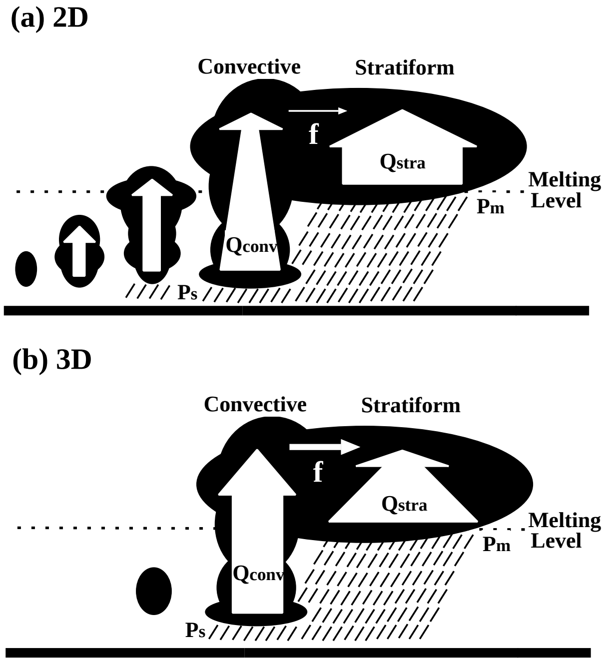

Figure 13: Schematic view of water budget of a mesoscale convective system in (a) 2D and (b) 3D simulations.

tems. Coarser resolution simulation produces the wider cloud width, which has a direct impact on clud entrainment, leading to fewer, more undilute convective cores that ascend higher unto the troposphere. Thus, the 3D model with coarser resolution is inherently limited in its ability to produce shallow convection and congestus-type clouds. More undilute convective cores produce more ice-phase condenstaes which are genereted in carried over from the convective region into stratiform region, and less condensate that is produced by the stratiform region's own upward motion (Fig. 13).

5. SUMMARY AND FUTURE WORK

Spectral Latent Heating (SLH) algorithm has been developed for the TRMM PR using the two-dimensional version of the GCE model. Real clouds and cloud systems are three-dimensional. The availability of exponentially increasing computer capabilities has resulted in three-dimensional CRM simulations for multiday periods with large horizontal domains becoming increasing prevalent. In this study, we compare look-up tables from the two- and three-dimensional CRM simulations.

The lookup table from GCE 3-D simulations results in less agreement between the SLH-retrieved Q_{1Rp} and sounding-based Q_1. The level of maximum heating of $Q_{1Rp} + Q_R$ is slightliy lower than that of the sounding-derived Q_1. This is explained by the fact that the 3D lookup table produces stronger convectiving heating and weaker stratiform heating above the melting level that 2D counterpart. Condensate generated in and carried over from the convective region is larger in 3D than in 2D, and condensate that is produced by the stratiform region's own upward motion is smaller in 3D than 2D.

Coarser resolution simulation produces the wider cloud width, which has a direct impact on clud entrainment, leading to fewer, more undilute convective cores that ascend higher unto the troposphere. More undilute convective cores produce more ice-phase condenstaes which are genereted in carried over from the convective region into stratiform region, and less condensate that is produced by the stratiform region's own upward motion. The 3D simulations with finer resolution (i.e. 250 m) is computationally expensive, because finer resolution requires small time step. The model domain is 64 km × 64 km for the 250 m simulation in Lang et al. (2007). Such small domain size is adequate for weakly organized convection exmamined in Lang et al. (2007), but inadequate for organized convection examined here. In the future, we will conduct the 3D simulations with finer resolution and large domain size, using a super computer.

Acknowledgement This study is supported by the JAXA/EORC Tropical Measuring Mission (TRMM) project.

REFERENCES

Awaka, J., T. Iguchi, and K. Okamoto: 1998, Early results on rain type classification by the Tropical Rainfall Measuring Mission (TRMM) precipitation radar. *Proc. 8th URSI Commission F Open Symp.*, URSI, Aveiro, Portugal, 143–146.

Chong, M. and D. Hauser: 1989, A tropical squall line observed during the COPT81 experiment in West Africa. Part II: Water budget. *Mon. Wea. Rev.*, **117**, 728–744.

Ciesielski, P. E., R. H. Johnson, P. T. Haertel, and J. Wang: 2003, Corrected TOGA COARE sounding humidity data: Impact on diagnosed properties of convection and climate over the warm pool. *J. Climate*, **16**, 2370–2384.

Donner, L. J., C. J. Seman, and R. S. Hemler: 1999, Three-dimensional cloud-system modeling of GATE convection. *J. Atmos. Sci.*, **56**, 1885–1912.

Fairall, C., E. F. Bradley, D. P. Rogers, J. B. Edson, and G. S. Young: 1996, Bulk parameterization of air-sea fluxes for TOGA COARE. *J. Geophy. Res.*, **101**, 3747–3764.

Gamache, J. F. and R. A. Houze Jr.: 1983, Water budget of a mesoscale convective system in the Tropics. *J. Atmos. Sci.*, **40**, 1835–1850.

Grabowski, W. W. and Coauthors: 2006, Daytime convective development over land: A model intercomparison based on LBA observations. *Quart. J. Roy. Meteor. Soc.*, **132**, 317–344.

Grabowski, W. W., X. Wu, M. W. Moncrieff, and W. D. Hall: 1998, Cloud-resolving modeling of tropical cloud systems during Phase III of GATE. Part II: Effects of resolution and the third spatial dimension. *J. Atmos. Sci.*, **55**, 3264–3282.

Houze, R. A., Jr.: 1982, Cloud clusters and large-scale vertical motions in the Tropics. *J. Meteor. Soc. Japan*, **60**, 396–410.

Iguchi, T., T. Kozu, R. Meneghini, J. Awaka, and K. Okamoto: 2000, Rain-profiling algorithm for the TRMM precipitation radar. *J. Appl. Meteor.*, **39**, 2038–2052.

Johnson, R. H. and P. E. Ciesielski: 2002, Characteristics of the 1998 summer monsoon onset over the northern South China Sea. *J. Meteor. Soc. Japan*, **80**, 561–578.

Johnson, R. H. and D. C. Kriete: 1982, Thermodynamic and circulation characteristics of winter monsoon tropical mesoscale convection. *Mon. Wea. Rev.*, **110**, 1898–1911.

Johnson, R. H. and G. S. Young: 1983, Heat and moisture budgets of tropical mesoscale anvil clouds. *J. Atmos. Sci.*, **40**, 2138–2146.

Kozu, T. and Coauthors: 2001, Development of precipitation radar onboard the Tropical Rainfall Measuring Mission (TRMM) satellite. *IEEE Trans. Geosci. Remote Sens.*, **39**, 102–116.

Lang, S., W.-K. Tao, R. Cifelli, W. Olson, J. Halverson, S. Rutledge, and J. Simpson: 2007, Improving simulations of convective systems from TRMM LBA: Easterly and westerly regimes. *J. Atmos. Sci.*, **64**, 1141–1164.

Leary, C. A. and R. A. Houze Jr.: 1979, Melting and evaporation of hydrometors in precipitation from the anvil clouds of deep tropical convection. *J. Atmos. Sci.*, **37**, 784–796.

Lin, X. and R. H. Johnson: 1996, Kinematic and thermodynamic characteristics of the flow over the western Pacific warm pool during TOGA COARE. *J. Atmos. Sci.*, **53**, 695–715.

Nitta, T. and S. Esbensen: 1974, Heat and moisture budget analyses using BOMEX data. *Mon. Wea. Rev.*, **102**, 17–28.

Okamoto, K.: 2003, A short history of the TRMM precipitation radar. *Cloud Systems, Hurricanes and the Tropical Rainfall Measurement Mission (TRMM): A Tribute to Dr. Joanne Simpson*, Amer. Meteor. Soc., number 51 in Meteor. Monogr., 187–195.

Schumacher, C. and R. A. Houze Jr.: 2003b, The TRMM precipitation radar's view of shallow, isolated rain. *J. Appl. Meteor.*, **42**, 1519–1524.

Shige, S., Y. N. Takayabu, and W.-K. Tao: 2008, Spectral retrieval of latent heating profiles from TRMM PR data. Part III: Estimating apparent moisture sink profiles over tropical oceans. *J. Appl. Meteor. Climatol.*, **47**, 620–640.

Shige, S., Y. N. Takayabu, W.-K. Tao, and D. E. Johnson: 2004, Spectral retrieval of latent heating profiles from TRMM PR data. Part I: Development of a model-based algorithm. *J. Appl. Meteor.*, **43**, 1095–1113.

Shige, S., Y. N. Takayabu, W.-K. Tao, and C.-L. Shie: 2007, Spectral retrieval of latent heating profiles from TRMM PR data. Part II: Algorithm improvement and heating estimates over tropical ocean regions. *J. Appl. Meteor. Climatol.*, **46**, 1098–1124.

Takayabu, Y. N.: 2002, Spectral representation of rain features and diurnal variations observed with TRMM PR over the equatorial area. *Geophys. Res. Lett.*, **29**, 1584, doi:10.1029/2001GL014113.

Tao, W.-K. and Coauthors: 2003, Microphysics, radiation and surface processes in the Goddard Cumulus Ensemble (GCE) model. *Meteor. Atmos. Phys.*, **82**, 97–137.

Tao, W.-K., S. Lang, J. Simpson, W. Olson, D. Johnson, B. Ferrier, C. Kummerow, and R. Adler: 2000, Vertical profiles of latent heat release and their retrieval for TOGA COARE convective systems using a cloud resolving vodel, SSM/I, and ship-borne radar data. *J. Meteor. Soc. Japan*, **78**, 333–355.

Tao, W.-K. and J. Simpson: 1993, Goddard cumulus ensemble model. Part I: Model description. *Terr. Atmos. Oceanic Sci.*, **4**, 35–72.

Tao, W.-K., J. Simpson, S. Lang, M. McCumber, R. Adler, and R. Penc: 1990, An algorithm to estimate the heating budget from vertical hydrometer profiles. *J. Appl. Meteor.*, **29**, 1232–1244.

Wang, Y., W.-K. Tao, and J. Simpson: 1996, The impact of ocean surface fluxes on a TOGA COARE cloud system. *Mon. Wea. Rev.*, **124**, 2753–2763.

Yanai, M., S. Esbensen, and J.-H. Chu: 1973, Determination of bulk properties of tropical cloud clusters from large-scale heat and moisture budgets. *J. Atmos. Sci.*, **30**, 611–627.

Yanai, M. and R. H. Johnson: 1993, Impacts of cumulus convection on thermodynamic fields. *The Representation of Cumulus Convection in Numerical Models*, Amer. Meteor. Soc., number 46 in Meteor. Monogr., 39–62.

Zeng, X. and Coauthors: 2007, Evaluating clouds in long-term cloud-resolving model simulations with observational data. *J. Atmos. Sci.*, **64**, 4153–4177.